



Investigation of the charges separation and transfer behavior of BiOCl/BiF₃ heterojunction



Yang Yang, Fei Teng*, Yandong Kan, Liming Yang, Zailun Liu, Wenhao Gu, An Zhang, Weiyi Hao, Yiran Teng

Jiangsu Engineering and Technology Research Center of Environmental Cleaning Materials (ECM), Jiangsu Collaborative Innovation Center of Atmospheric Environment and Equipment Technology (CICAET), Jiangsu Key Laboratory of Atmospheric Environment Monitoring and Pollution Control (AEMPC), Jiangsu Joint Laboratory of Atmospheric Pollution Control (APC), School of Environmental Science and Engineering, Nanjing University of Information Science & Technology, 219 Ningfu Road, Nanjing 210044, China

ARTICLE INFO

Article history:

Received 8 October 2016

Received in revised form

10 December 2016

Accepted 25 December 2016

Available online 26 December 2016

Keywords:

Charge transfer

Surface electric field

Bulk internal electric field

Interface electric field

ABSTRACT

To date, it is still a big challenge to investigate the charge transfer behavior from bulk to surface for the solar energy conversion and utilization. Herein, the BiF₃/BiOCl heterojunction has been prepared through a mild post-synthesis method. Surface photovoltage spectra (SPV) results show that only negative SPV signal can be observed for BiOCl, suggesting that the photogenerated electrons mainly move to the surfaces and accumulate on the surface; both negative and positive signals can be observed for 38% BiF₃/BiOCl, indicating that photogenerated electrons and holes can both move to the surfaces and accumulate on the surface; but nearly no SPV signal can be observed for BiF₃, demonstrating that nearly no electrons or holes can accumulate on the surface. Furthermore, under ultraviolet light irradiation ($\lambda \leq 420$ nm), the degradation rate is 5.3 and 5.8 times higher than that of BiOCl and BiF₃ for the degradation of 2-nitrophenol, respectively. We hold that the charges transfer and separation efficiency of BiF₃/BiOCl have been significantly improved by the synergistic effect of the surface electric field, bulk internal electric field and interface electric field. This work could help us to intensively understand the charge transfer behavior of a heterojunction photocatalyst.

© 2016 Elsevier B.V. All rights reserved.

1. Introduction

The conversion and utilization of solar energy, e.g., photocatalysis, has caused great attention because of its potential application in energy conversion, purifying wastewater and noxious gas [1–5]. Many semiconductors have been developed to meet the demand for practical application, such as TiO₂ [1], ZnO [6,7], Ag₃PO₄ [8–10], CdS [11] and so on. However, the low charge separation efficiency limits the application in practices. Currently, bismuth-based semiconductors, including BiVO₄ [12,13], BiWO₄ [14], Bi₃PO₄ [15], Bi₂O₂CO₃ [16,17], BiOX (X = Cl, Br, I) [18–21], etc. have shown efficient photocatalytic activities in wastewater and noxious gas purification. Among them, layer structured BiOCl (composed of [Bi₂O₂]²⁺ layers interleaved with Cl layers) have attracted great interests due to its outstanding optical and electrical properties [22,23]. However, its photocatalytic activity is obviously limited by the wide band gap and high recombination rate of photogenerated car-

ries [24,25]. Moreover, it is still a big challenge to investigate the charge transfer behavior of photocatalysts. Up to now, many efforts have been made to enhance the photocatalytic performance of BiOCl, such as metal doping (Fe, Zn, Cu, Mn, etc.) [23,26–28], non-metal doping (F, C, etc.) [19,29], co-catalyst modification (Ag, Au, Bi etc.) [30–35] and semiconductor heterojunctions (BiO/BiOCl [36], Bi₂S₃/BiOCl [37], Ag/AgX/BiOX [21,38], BiOCl/Ag₃PO₄ [39], g-C₃N₄/BiOCl [25,40], Bi₂O₂CO₃/BiOCl [41], TiO_{2-x}/BiOCl [42], etc.). Among the various strategies, heterojunction is one of the most efficient strategies for the enhancement of photocatalytic activity [43] because the low charge transfer and separation is one of the most impediments for photocatalysis. Recently, BiF₃ have been reported as a new, efficient photocatalyst in our group [44], which has a highly positive valence band (6.04 eV) and an excellent electrical conductivity. Moreover, BiF₃ has the matched energy bands with BiOCl [45]. We expect that compared with BiF₃ and BiOCl, BiF₃/BiOCl heterojunction may have an improved activity, which has not been reported yet.

Herein, a mild post-synthesis method has been developed to prepare BiF₃/BiOCl heterojunction by using BiOCl and NH₄F as the precursors. A plausible conversion mechanism has been proposed.

* Corresponding author.

E-mail address: tfwd@163.com (F. Teng).

The physical properties of as-obtained samples are characterized by X-ray diffraction (XRD), scanning electron microscopy (SEM), high-resolution transmission electron microscopy (HRTEM), selected area electron diffraction (SAED), UV-vis diffuse reflectance spectroscopy (UV-DRS) and N_2 sorption isotherms. Additionally, the charge behaviors of samples are measured by electrochemical impedance spectroscopy (EIS), and photoluminescence (PL) spectra. The surface charge behavior is mainly revealed by the surface photovoltage spectra (SPV) [46,47]. In addition, the photocatalytic performances of the samples were tested by the degradation of methyl orange (MO) and 2-nitrophenol aqueous solutions [42,48]. The capturing experiments were also performed to investigate the main active oxidative species [40,49]. We expect that this work could help us to intensively understand the charge transfer behavior of photocatalysts.

2. Experimental

2.1. Sample preparation

All reagents were of analytical grade, purchased from Beijing Chemical Reagents Industrial Company of China, and were used without further purification.

2.1.1. Preparation of $BiOCl$

$BiOCl$ sample was prepared according to our previously reported method [45]. Typically, 1.5 mmol of $Bi(NO_3)_3 \cdot 5H_2O$ was dissolved in 30 mL of ethylene glycol (EG) under stirring at room temperature. After the $Bi(NO_3)_3 \cdot 5H_2O$ was completely dissolved, 10 mmol of NaCl was added to the above solution. After being stirring for 30 min, the solution was transferred into a 50-mL Teflon-lined stainless steel autoclave, and then maintained at 170 °C for 6 h. After reaction, the autoclave was cooled to room temperature naturally. The resulting sample was centrifuged and washed with ethanol and distilled water three times, and then dried at 60 °C for 3 h. The obtained sample was designated as BF-0.

2.1.2. Preparation of $BiF_3/BiOCl$ and BiF_3

Typically, 1 mmol as-obtained $BiOCl$ (0.2605 g) above was dispersed into a 20 mL of ethanol, then, 1, 2, 4 and 6 mmol NH_4F was added into the solution above, respectively. After being stirring for 30 min, the mixture solutions was transferred to Teflon-lined stainless steel autoclave, and maintained at 170 °C for 6 h. The resulting precipitate was centrifuged, washed with ethanol and distilled water for three times and dried at 60 °C for 3 h. The as-obtained samples at 1, 2, 4 and 6 mmol of NH_4F were designated as BF-1, BF-2, BF-3 and BF-4, respectively.

2.2. Characterization

The crystal structures of the samples were determined by X-ray powder polycrystalline diffractometer (XRD, Rigaku D/max-2550VB), using graphite monochromatized $Cu K\alpha$ radiation ($\lambda = 0.154$ nm), operating at 40 kV and 50 mA. The XRD patterns were obtained in the range of 10–80° (2 θ) at a scanning rate of 7° min⁻¹. The samples were characterized by a scanning electron microscope (SEM, Hitachi SU-1510) with an acceleration voltage of 15 keV. The samples were coated with 5-nm-thick gold layer before observations. The fine surface structures of the samples were determined by high-resolution transmission electron microscopy (HRTEM, JEOL JEM-2100F) equipped with an electron diffraction (ED) attachment with an acceleration voltage of 200 kV. Nitrogen sorption isotherms were performed at 77 K and $<10^{-4}$ bar on a Micromeritics ASAP2010 gas adsorption analyzer. Each sample was degassed at 150 °C for 5 h before measurements. Surface area

was calculated by the Brunauer-Emmett-Teller (BET) method. UV-diffused reflectance spectra of the samples were obtained using a UV-spectrophotometer (UV-2550, Shimadzu, Japan). $BaSO_4$ was used as a reflectance standard in a UV-vis diffuse reflectance experiment. All the electrochemical measurements were carried out on a CHI 660D electrochemical working stations at room temperature. For a standard three-electrode cell, a 0.2 M Na_2SO_4 aqueous solution was used as the electrolyte. ITO (with an area of 2 cm²) was used as the current collector of working electrode for detecting photocurrent response and Ni film (with an area of 1 cm²) was used as the current collector of working electrode for testing EIS. Pt wire (diameter: 0.1 cm, length: 4 cm) and Hg/HgO (S.C.E) electrodes were used as the counter and reference electrodes. To fabricate the working electrode, 80 wt% of active materials, 10 wt% of acetylene black (conductive agent) and 10 wt% of vinylidene fluoride (binder) were dispersed in 1-methyl-2-pyrrolidinone to form homogeneous slurry. Then the slurry was dotted on the ITO or Ni film and dried for 24 h at room temperature. Electrochemical impedance spectroscopy (EIS) was performed from 0.01 Hz to 100 kHz at an open circuit potential of 0.3 V and alternating current (AC) voltage amplitude of 5 mV. The photo electrodes were prepared by a dip-coating method and 0.2 M Na_2SO_4 was used as the electrolyte solution. The data were analyzed by ZSimWin software. The photoluminescence (PL) spectra were obtained on Cary Eclipse fluorescence spectrophotometer at room temperature under the 265 nm laser excitation (Cary Eclipse, Agilent).

2.3. Surface photovoltage (SPV) measurement

Surface photovoltage (SPV) measurement system [46,47] is consist of a monochromatic light source, a lock-in amplifier (SR830-DSP) with a light chopper (SR540), a photovoltaic cell and a computer. The monochromatic light is provided by a 500 W xenon lamp (CHFXQ500 W, Global Xenon Lamp Power) and a double-prism monochromator (Zolix SBP500). During the SPV measurement, the samples were test without further treatment. While the measurement of surface photovoltage was performed, the contact between the samples and the indium tin oxide (ITO) electrode was not ohmic. The construction of the photovoltaic cell is a sandwich like structure, which consist of steel timber, sample and ITO. We placed the powders on the steel timber electrode, then, the powder was pressed to obtain a film with ITO electrode.

2.4. Evaluation of photocatalytic activity

The photodegradation reactions of methyl orange (MO) and 2-nitrophenol were carried out to evaluate the catalytic activities under ultraviolet light irradiation ($\lambda \leq 420$ nm), using a 500 W Xe arc lamp (CEL-HXF 300) equipped with a cutoff filter ($\lambda > 420$ nm) as a light source. Typically, 0.1 g of powders was suspended in 200 mL aqueous solution of MO (12.5 mg L⁻¹) or 2-nitrophenol (4.5 mg L⁻¹) under continuous magnetic stirring. Before light-on, the suspension was stirred for 30 min to reach an adsorption-desorption equilibrium of organic molecules on the photocatalyst surface. During reaction, 3 mL of suspension was collected at a given interval time and centrifuged to remove the powders. The concentration of pollutant was determined by using UV-vis spectrophotometer. Herein, the degradation efficiency of MO and 2-Nitrophenol can be simplified as a pseudo-first-order kinetic reaction, and the apparent reaction rate constants (k_a) are calculated by the formula (4) as follows [42,48].

$$\ln(C_0/C) = k_a t \quad (1)$$

where C is the concentration of MO and 2-nitrophenol remaining in solution at different irradiation time, and C_0 is the initial concentration before irradiation.

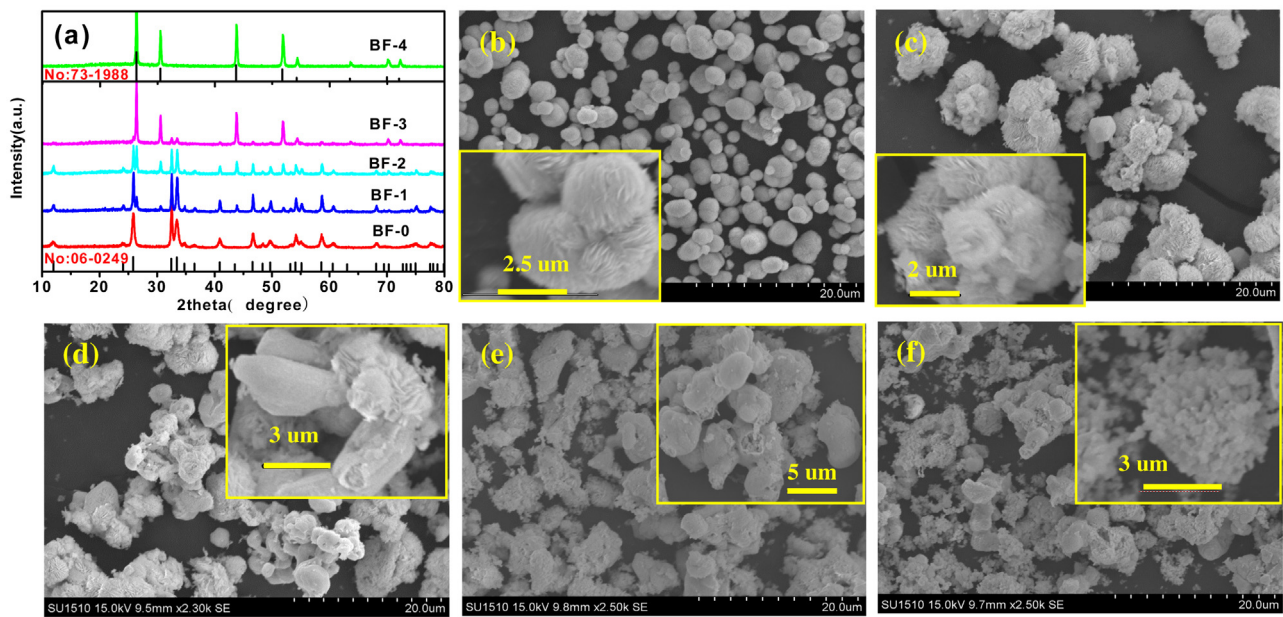


Fig. 1. X-ray diffraction (XRD) patterns (a) and scanning electron microscopy (SEM) images (b–f) of the samples: (b) BF-0 (BiOCl); (c) BF-1 ($\text{BiF}_3/\text{BiOCl}$); (d) BF-2 ($\text{BiF}_3/\text{BiOCl}$); (e) BF-3 ($\text{BiF}_3/\text{BiOCl}$); (f) BF-4 (BiF_3).

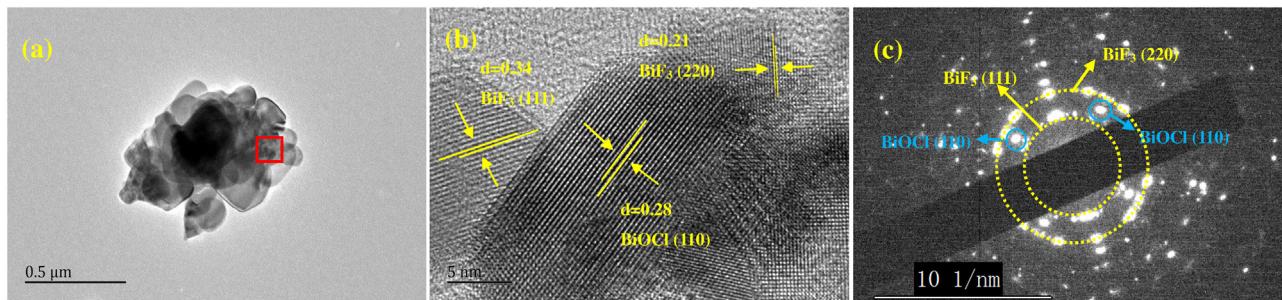


Fig. 2. High-resolution transmission electron microscopy (HRTEM) images and selected-area electron diffraction (SAED) patterns of BF-1 ($\text{BiF}_3/\text{BiOCl}$).

In order to investigate the active species, ammonium oxalate, isopropyl alcohol (IPA) and benzoquinone (BQ) were employed as the scavengers to capture holes (h^+), hydroxyl radicals ($\cdot\text{OH}$) and superoxide radical ($\cdot\text{O}_2^-$), respectively [40,49,50]. The other procedures were same as above.

3. Results and discussion

3.1. Effect of Bi/F molar ratio on the samples

Fig. 1a shows the XRD patterns of the samples. All the diffraction peaks of the as-prepared BF-0 sample are in good agreement with the standard BiOCl (JCPDS No. 06-0249), indicating the phase-pure BiOCl is formed. At Bi: F = 1: 1, 1: 2 and 1: 4, BiF_3 (No. 73-1988) form besides BiOCl, indicating that a part of BiOCl has converted into BiF_3 ; Moreover, the peak intensities of BiF_3 (at $2\text{Theta} = 30.5^\circ, 43.6^\circ$ and 51.7°) increase with increasing the amount of NH_4F added. At Bi: F = 1: 6, the XRD patterns of BF-4 sample are in accordance with the standard BiF_3 (No. 73-1988), which indicates that the phase-pure BiF_3 has formed. The SEM images of the samples are shown in Fig. 1(b–f). The as-prepared BiOCl sample is composed of the microspheres assembled by the nanosheets with the diameters of 4–7 μm . After treated by NH_4F , the microspheres have obviously broken into nanosheets, and some of irregular particles have formed (Fig. 1(c–f)). When NH_4F is substituted by NaF , however, the as-obtained sample is still the phase-pure BiOCl (Fig. S1a, in sup-

porting information (SI)). These results above indicate that NH_4F has a significant impact on the phase composition and morphology of the sample.

In ethanol, the reaction between BiOCl and NH_4F is like a solution–solution reaction, because both BiOCl and NH_4F could dissolve in ethanol. Herein, we assume that NH_4^+ , as a Lewis acid, can destroy the $[\text{Bi}_2\text{O}_2]$ layers. At lower amount of NH_4F added (Bi:F = 1:1, 1:2 and 1:4), the $[\text{Bi}_2\text{O}_2]$ slabs may have been partially destroyed, so tetragonal BiOCl has partially converted into cubic BiF_3 . As a result, $\text{BiF}_3/\text{BiOCl}$ heterojunctions have formed. Further increasing the amount of NH_4F (Bi:F = 1:6) added, the $[\text{Bi}_2\text{O}_2]$ slabs may have been destroyed completely. As a result, tetragonal BiOCl has completely converted into cubic BiF_3 treated by NH_4F in the medium of ethanol solution. However, NaF is insoluble in ethanol, so the reaction is via a solid–solution reaction. In addition, the $[\text{Bi}_2\text{O}_2]$ layers cannot be destroyed by NaF , hence, BiOCl can not convert to BiF_3 or BiOF . When we substitute ethanol for distilled water as the reaction medium (NH_4F), nevertheless, BiOCl has converted into BiOF , instead of BiF_3 (Fig. S1b, SI). We hold that when water is employed as the medium, a solid–solution reaction mainly occurs. In the presence of NH_4^+ ($\text{NH}_4^+ + \text{H}_2\text{O} \rightarrow \text{NH}_3 \cdot \text{H}_2\text{O} + \text{H}^+$), BiOCl solids could dissolve partially. As a result, BiOCl, $[\text{Bi}_2\text{O}_2]^{2+}$ and Cl^- may be present simultaneously in aqueous solution. Moreover, F^- will gradually replace Cl^- to form BiOF crystal due to a strong electronegativity of F^- . It should be noted that the real conversion

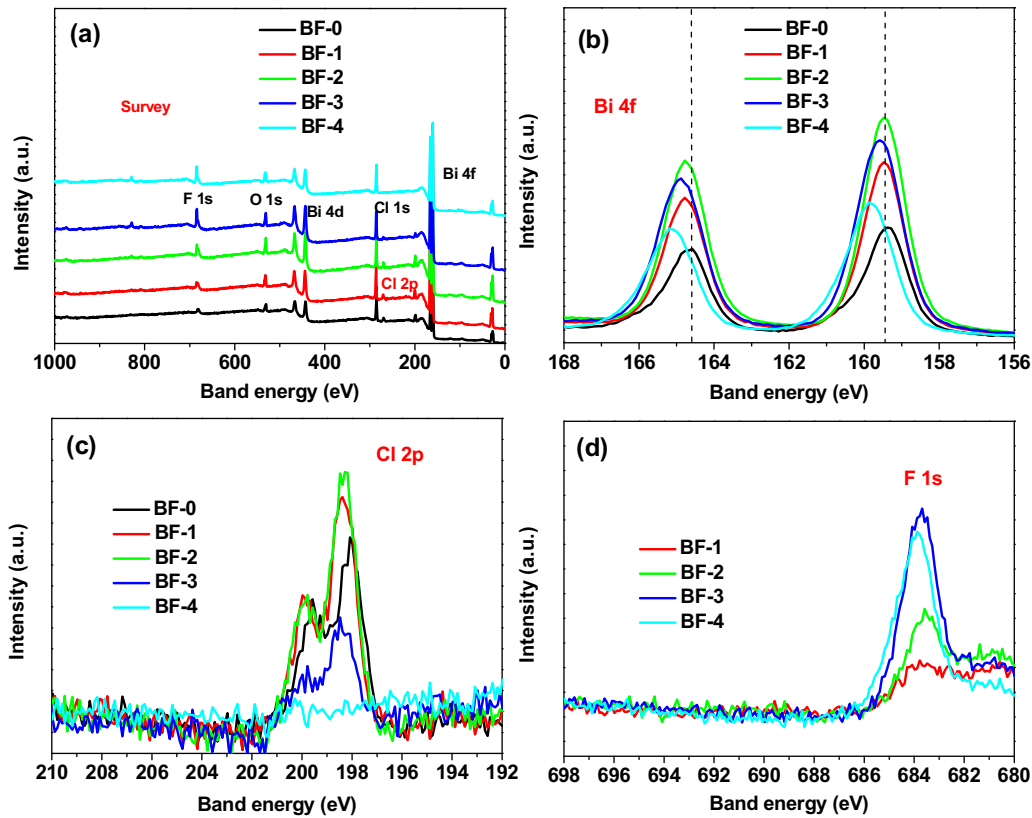


Fig. 3. XPS spectra of as-prepared samples: (a) Wide scan (survey); (b) Bi 4f; (c) Cl 2p; (d) F 1s.

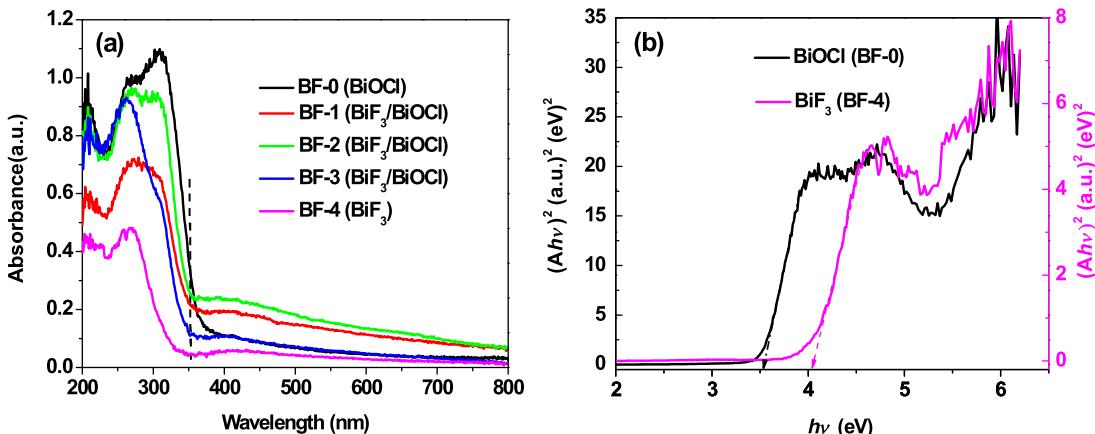


Fig. 4. (a) Ultraviolet-visible diffuse reflectance spectra (UV-DRS) of the samples; (b) Tauc plots (Absorption² vs. energy) of BiOCl and BiF₃ samples.

mechanism still needs further investigation. However, this conversion process is mild and meaningful to obtain new materials.

Further, BF-1 sample is typically characterized by the high-resolution transmission electron microscopy (HRTEM) and selected-area electron diffraction (SAED) patterns (Fig. 2). Fig. 2a shows that the nanoparticles distribute on the nanosheets. As shown in Fig. 2b, the lattice spacing of 0.28 nm is close to the (110) plane (0.275 nm) of BiOCl [45], and the lattice spaces of 0.21 and 0.34 nm well match the (220) (0.207 nm) and (111) (0.338 nm) planes of BiF₃, respectively. Additionally, Fig. 2c shows that the clear diffraction spots correspond to the (110) Bragg reflections of single-crystal BiOCl, and the diffraction rings correspond to (111) and (220) Bragg reflections of polycrystalline BiF₃, respectively. The results above firmly confirm the formation of BiF₃/BiOCl heterojunction.

3.2. Optical and charge transfer properties of the samples

We have investigated the optical and charge transfer properties of the samples by XPS, UV-DRS, EIS, Photocurrent, PL and SPV.

3.2.1. XPS analysis

XPS analysis was employed to explore surface chemical state and composition of the samples. From the survey spectrum shown in Fig. 3a, the peaks of Bi, O and Cl can be found for BF-0, BF-1, BF-2 and BF-3 samples. However, the peaks of F can be found for BF-1, BF-2, BF-3 and BF-4 samples. In Fig. 3b, two main peaks with the binding energies at about 158–160 eV and 164–166 eV are corresponding to the Bi 4f_{7/2} and Bi 4f_{5/2} of Bi³⁺, respectively [22]. It is noteworthy that the band energies of Bi³⁺ in BF-4 (BiF₃) are slightly higher than that of BF-0 (BiOCl) sample. Hence, compared with BF-

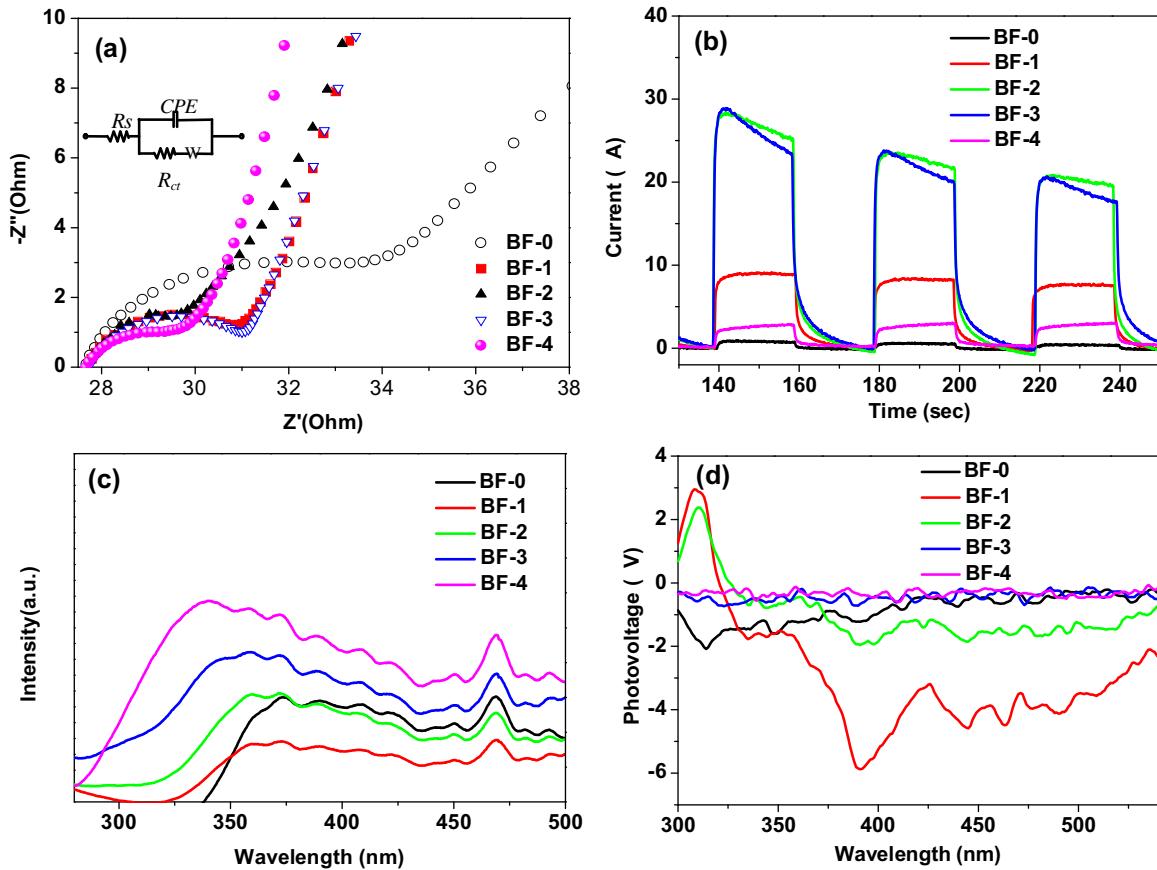


Fig. 5. (a) EIS Nyquist plots of samples; (b) Transient photocurrent densities of samples under ultraviolet light irradiation ($\lambda \leq 420$ nm); (c) PL spectra of the samples excited by 265-nm light; (d) Surface photovoltaic spectra (SPV) of samples.

Table 1

Atomic concentration (atom %) and the molar ratios of BiF_3 to BiOCl of the samples.

Species Samples	Phase composition	Cl 2p	F 1s	${}^*\text{BiF}_3/\text{BiOCl}$
BF-0	BiOCl	/	/	/
BF-1	$\text{BiF}_3/\text{BiOCl}$	26%	30%	38%
BF-2	$\text{BiF}_3/\text{BiOCl}$	24%	47%	65%
BF-3	$\text{BiF}_3/\text{BiOCl}$	14%	69%	165%
BF-4	BiF_3	/	/	/

*Notes: Calculated molar ratios from XPS results.

0, the blue shifts occur in BF-1, BF-2, BF-3 indicates the increased amounts of BiF_3 . In Fig. 3c, the peaks at about 198.5 and 199.8 eV could be ascribed to $\text{Cl} 2p_{3/2}$ and $\text{Cl} 2p_{1/2}$ for BF-0, BF-1, BF-2 and BF-3 samples, respectively [43]. Fig. 3d shows that the F 1s spectrum could be observed at about 683.5 eV for BF-1, BF-2, BF-3 and BF-4 samples. The above results also demonstrate that BiOCl could be converted to BiF_3 eventually with increasing NH_4F . Additionally, Table 1 summarizes the calculated mole percents of Cl and F. The XPS spectra of O 1s are shown in Fig. S2. According to the molar ratios of F and Cl, we can obtain the approximate molar ratios of BiF_3 to BiOCl of the samples, also given in Table 1. From the calculated results, the molar ratios of BiF_3 to BiOCl are about 38%, 65% and 165% for BF-1, BF-2 and BF-3 samples, respectively. Additionally, EDS is also employed to analyze the molar ratios of BiF_3 and BiOCl , which have been discussed in supporting information (Section 1.1, SI). The results show that the elements contents are different from the XPS and EDS results (Table S1 and Fig. S3) demonstrating the distribution of BiF_3 and BiOCl are not uniform.

Table 2

The band gap (E_g), VBM (E_{VB}) and CBM (E_{CB}) of the samples.

Chemicals	χ (eV)	E_g (eV)	E_{VB} (eV)	E_{CB} (eV)
BiOCl	6.65	3.51	3.91	0.40
BiF_3	8.53	4.02	6.04	2.02

Notes: χ , the geometric mean of Mulliken's electronegativities; VBM, valence band maximum; CBM, conduction band minimum.

3.2.2. UV-DRS analysis

Fig. 4a displays the UV-visible diffuse reflectance spectra (UV-DRS) of the samples. All the samples exhibit the light absorption in UV light ranges. The absorption edges of BF-0 (BiOCl), BF-1 (38% $\text{BiF}_3/\text{BiOCl}$), BF-2 (65% $\text{BiF}_3/\text{BiOCl}$), BF-3 (165% $\text{BiF}_3/\text{BiOCl}$) and BF-4 (BiF_3) are determined to be about 353, 350, 348, 345 and 310 nm, respectively. The band gaps of BF-0, BF-1, BF-2, BF-3 and BF-4 are 3.51, 3.54, 3.56, 3.59 and 4.02 eV, respectively. Compared with BiOCl , all the treated samples show obvious blue-shifts and the increased band gaps. In addition, the band gap of semiconductors also can be calculated by Kubelka–Munk (KM) expression [51]:

$$\alpha h\nu = A(h\nu - E_g)^{n/2} \quad (2)$$

where α , h , ν , A and E_g are absorption coefficient, Planck's constant, photon frequency, proportionality constant and band gap, respectively. According to the plots of $(\alpha h\nu)^2$ vs. photo energy (Fig. 4b), the band gaps of BiOCl and BiF_3 are calculated to be 3.51 and 4.02 eV, respectively. It is worth noting that BF-1 and BF-2 samples show the enhanced absorption abilities than other samples in the wavelength range from about 350–800 nm.

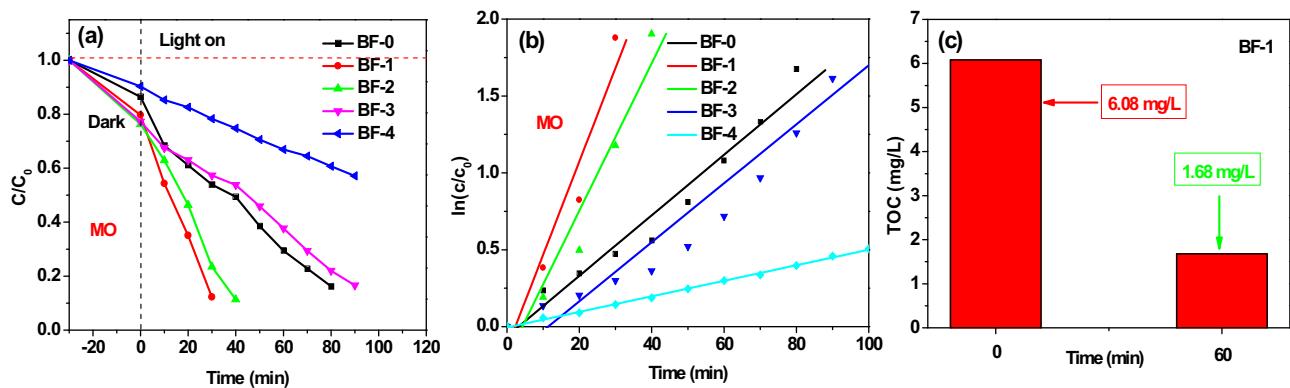


Fig. 6. Degradation curves (a), reaction kinetic curves (b) and TOC image (c) of MO over the samples under ultraviolet light irradiation ($\lambda \leq 420$ nm).

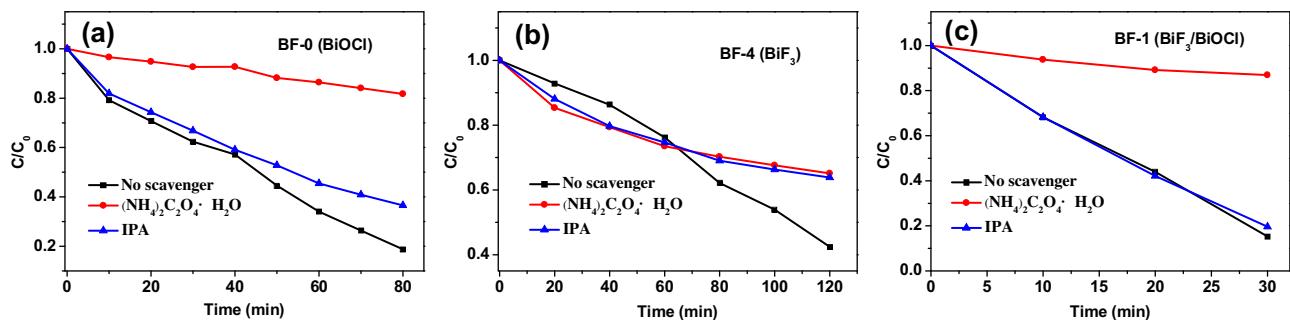


Fig. 7. Degradation curves of MO over the samples under UV light irradiation ($\lambda \leq 420$ nm): (a) BF-0 (BiOCl); (b) BF-4 (BiF₃); (c) BF-1 (BiF₃/BiOCl).

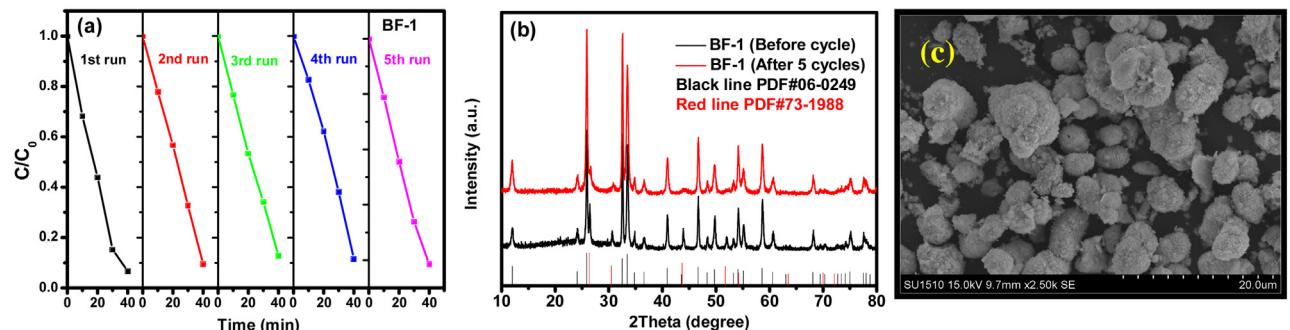


Fig. 8. (a) Cycle curves of MO over BF-1 sample under UV light irradiation ($\lambda \leq 420$ nm); (b) XRD patterns of BF-1 before and after 5 cycles under UV light irradiation ($\lambda \leq 420$ nm); (c) SEM image of BF-1 after 5 cycles.

Further, the conduction and valence band positions (E_{CB} , E_{VB}) of a semiconductor can be calculated by the following empirical formula [52]:

$$E_{VB} = \chi - E^e + 0.5E_g \quad (3)$$

$$E_{CB} = E_{VB} - E_g \quad (4)$$

where χ is the absolute electronegativity of a semiconductor, which is defined as the geometric mean of the absolute electronegativity of constituent atoms; E^e is the energy of free electrons on the hydrogen scale (ca. 4.5 eV). The specific calculation processes are shown in supporting information (Section 1.2, SI). Herein, the calculated E_{CB} and E_{VB} values of BiOCl and BiF₃ samples are summarized in Table 2. It is obvious that the CB (0.4 eV) of BiOCl lies above that (2.02 eV) of BiF₃, while the VB (6.04 eV) of BiF₃ lies below that (3.91 eV) of BiOCl. This suggests that a stable heterojunction can form between BiF₃ and BiOCl.

3.2.3. EIS analysis

Fig. 5a shows the electrochemical impedance spectra (EIS) of the samples. It is well known that the smaller arc radius indicates a higher electrical conductivity, which will favors for an efficient electron transfer [16,53,54]. The simulated equivalent electric circuit from EIS Nyquist plots consists of a solution resistance (R_s), a constant phase element (CPE) accounting for electrical double-layer capacitance, a charge-transfer resistance (R_{ct}), and a Warburg impedance (W) for the diffusion and insertion of ion into active materials. The R_{ct} values of BiOCl, BF-1, BF-2, BF-3 and BF-4 (BiF₃) are calculated to be 2.83, 1.85, 2.54, 2.32 and 0.46 Ω , respectively. This clearly demonstrates the charge-transfer resistance (R_{ct}) of BiF₃ is obviously smaller than BiOCl, and the charge-transfer ability of all BiF₃/BiOCl heterojunctions are higher than BiOCl, but lower than BiF₃. We believe that the formed interfacial electric field between BiOCl and BiF₃ is the crucial factor for the enhanced transfer and separation efficiency of photogenerated charges, which will improve its photocatalytic activity.

3.2.4. Photocurrent analysis

Additionally, photocurrent response spectrum is an important method to investigate the interfacial charge separation and transfer efficiency [16,55]. Herein, the photocurrent response spectra of the samples are performed under UV-light irradiation ($\lambda \leq 420$ nm). As shown in Fig. 5b, BF-4 (BiF₃) sample shows a higher charge separation dynamics than BF-0 (BiOCl). Moreover, BiF₃/BiOCl heterojunctions show much higher separation efficiencies than BiOCl and BiF₃.

3.2.5. PL analysis

As is known, the photoluminescence (PL) spectroscopy has been widely used to investigate the optical properties and the recombination rate of electrons and holes pairs [55]. Fig. 5c shows PL spectra of the samples with the excitation wavelength of 265 nm. The PL intensity of BF-1 sample is much lower than those of the other samples, indicating that the lower recombination efficiency of photogenerated carriers could favor for the improvement of photocatalytic activity.

3.2.6. SPV analysis

Fig. 5d shows the SPV spectra of the samples. BF-0 (BiOCl) exhibits a negative SPV signal in the range of 300–425 nm, indicating that the photogenerated electrons move from the bulk to the surface of BiOCl, and the photogenerated holes migrate from the surface to the bulk [46]. For BF-3 and BF-4 (BiF₃) samples, only much weak negative SPV signals can be observed, which means that only fairly fewer photogenerated electrons can move to the surfaces of the samples. This would result in poor photocatalytic performance. However, both intensive positive and negative signals are observed for BF-1 and BF-2 samples, indicating that both electrons and holes can move to the surfaces and accumulate under different wavelength light illuminating. The similar results have been observed in BiVO₄ heterophase composites reported by Fan et al. [47]. As shown in Fig. S4, when the wavelength of incident light is in the range of 320–353 nm, only BiOCl can be excited, but BiF₃ can not. In this case, the generated electrons of BiOCl cannot move to the BiF₃, and the BiF₃/BiOCl heterojunction only shows a negative SPV signal that mainly results from BiOCl.

From the UV-DRS (Fig. 4a), we can see that both the BF-1 and BF-2 samples still have a small light absorption at the wavelength of 353–500 nm, which can attribute to the sub-gap transition [56]. It is well known that the light absorbed by shallow energy level and surface state can result in the sub-gap transition [56,57]. Herein, the shallow energy levels of a semiconductor are the electronic bound states close to conductive band bottom and/or the hole bound states close to valence band top. Under light irradiation or heating, the electrons and/or holes are easy to ionize and escape from shallow energy levels, then become the free electrons in CB and/or the free holes in VB [57]. For a semiconductor, the surface states are ubiquitous due to dangling chemical bond on the solid surfaces caused by periodic crystal lattice interruption, or defects, or adsorbed impurities on the crystal surface. These surface states (surface energy levels) can also bound electrons or holes [58,59].

On one hand, while being irradiated by the incident light (353–500 nm), the electrons or holes in the shallow energy level of BiF₃/BiOCl interfaces (BF-1 and BF-2) would absorb the photons, then escape from the shallow energy level and become the free electrons in conduction band or free holes in valence band. With the separation of electrons and holes in the shallow energy levels, the SPV signal would be generated. On the other hand, the visible emission also occurred in ZnO with a band gap of 3.2 eV, which has been attributed to the surface defect states [57]. Hence, we hold that the surface state of material also contributes to the generation of SPV signal at the wavelengths of 353–500 nm.

Table 3

BET areas and apparent rate constants (k_a) of the samples for the degradation of methyl orange (MO) and 2-Nitrophenol under ultraviolet light irradiation ($\lambda \leq 420$ nm).

Samples	BiOCl	BF-1	BF-2	BF-3	BiF ₃
BET (m^2g^{-1})	16.5	12.5	10.1	7.0	4.2
k_a1 (MO, min^{-1})	0.0197	0.0607	0.0479	0.0192	0.0051
k_a2 (2-Nitrophenol, min^{-1})	0.0097	0.0516	0.0553	0.0200	0.0088

Notes: BET areas, calculated by the Brunauer-Emmett-Teller (BET) method.

Summarily, we hold that the SPV signals at the wavelength of 353–500 nm are result from the light absorption by shallow energy level and surface state. Under the UV light irradiation (300–320 nm), however, both BiOCl and BiF₃ can be excited. Hence, the generated electrons on the CB of BiOCl would move to the CB of BiF₃, and the generated holes on the VB of BiF₃ would transfer to that of BiOCl. As a result, the BiF₃/BiOCl heterojunction is efficient, which benefits the charges transfer. When the holes move to surface of BiOCl, the positive SPV signal occurred.

3.3. Photocatalytic activities of the samples

Fig. 6(a,b) shows the degradation curves and reaction kinetic curves of methyl orange (MO) dye under UV light irradiation ($\lambda \leq 420$ nm). The degradation activities of the samples follow the order as follows: BF-1 > BF-2 > BF-0 > BF-3 > BF-4. After being irradiated for 30 min, nearly 90% and 77% of MO have been degraded by BF-1 and BF-2 samples, respectively; however, only 46%, 43% and 22% of MO have been degraded by BF-0 (BiOCl), BF-3 and BF-4 (BiF₃), respectively. The degradation rate constants (k_a) are given in Table 3. The degradation rate constant ($k_a = 0.0607 \text{ min}^{-1}$) of BF-1 sample is 3.08 and 11.9 times higher than those of the untreated BiOCl ($k_a = 0.0197 \text{ min}^{-1}$) and BiF₃ ($k_a = 0.0051 \text{ min}^{-1}$), respectively. It is obvious that the 38% BiF₃/BiOCl heterojunction (BF-1) shows the highest activity than the others for the degradation of MO. Additionally, the photocatalytic activities of the sample synthesized in Bi:F = 1:0.5 and commercial P25 were shown in Fig. S5 and S6. From Fig. S5b, we can see that the photocatalytic activity of BF-1 is better than that of the sample synthesized at Bi:F = 1:0.5, but slightly lower than that of commercial P25 (Fig. S6). Fig. 6c shows the total organic carbon (TOC) variation over BF-1 sample for the degradation of MO. Before light irradiation, the initial TOC content is 6.08 mg/L; after being irradiated for 30 min the TOC content has decreased to 1.68 mg/L. The result suggests that the nearly 72.4% of MO molecules has been completely degraded into CO₂ and H₂O. As shown in Table 3, the BET areas of the samples follow the order of BF-0 > BF-1 > BF-2 > BF-3 > BF-4. However, their photocatalytic activities follow the order of BF-1 > BF-2 > BF-0 > BF-3 > BF-4. This indicates that the BET area may not be the vital factor for their photocatalytic activities. According to the results of Fig. 5, we assume that the improved activity of BF-1 may mainly result from the formation of BiF₃/BiOCl heterojunctions, which would benefit the separation and transfer rate of photogenerated charges.

3.3.1. Trapping experiment

Typically, we have conducted the trapping experiments of MO dye over BF-0 (BiOCl), BF-1 (38% BiF₃/BiOCl) and BF-4 (BiF₃) samples, in which ammonium oxalate and isopropyl alcohol (IPA) are used as the hole scavenger and the hydroxyl radical scavenger, respectively. In Fig. 7a, the photocatalytic activity of BiOCl (BF-0) decreases slightly, when the 20 mL IPA is added into the solution; while the photocatalytic activity obviously decreases when 1 mmol ammonium oxalate added. For BiF₃ (BF-4) sample, the IPA and ammonium oxalate have a similar effect on the photocatalytic activity, as shown in Fig. 7b. As for BF-1 (38% BiF₃/BiOCl)

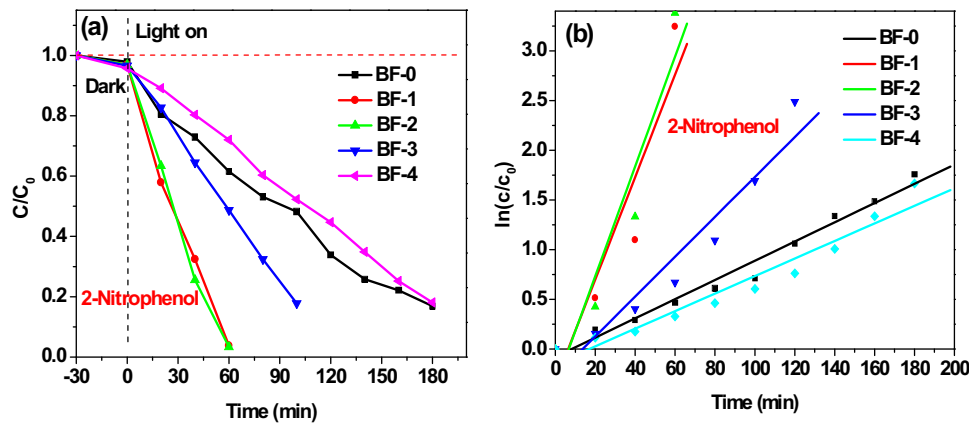


Fig. 9. Degradation curves (a) and reaction kinetic curves (b) of 2-nitrophenol over the samples under ultraviolet light irradiation ($\lambda \leq 420$ nm).

sample, we can see that the photocatalytic activity was obviously inhibited by ammonium oxalate, while IPA nearly does not affect the photocatalytic activity (Fig. 7c). The superoxide radical ($\cdot\text{O}_2^-$) trapping experiment is shown in Fig. S7 (supporting information). The results show that the photocatalytic activity of BF-1 sample is greatly inhibited by adding 2 mg benzoquinone (BQ), indicating superoxide radical is also the major active species. Zheng et al. have confirmed that the superoxide radical can directly degrade MO by trapping experiments and ESR results [50]. The results above indicate that the photogenerated holes is the major active oxidative specie for BiOCl (BF-0) sample, while both hydroxyl radicals and holes are the major active oxidative species for BiF₃ (BF-4) sample. However, the MO degradation over BF-1 (BiF₃/BiOCl heterojunction) was driven mainly by the superoxide radicals and holes.

3.3.2. Cycle stability

In order to investigate the stability of BiF₃/BiOCl heterojunction (BF-1) sample, we have further performed the cycle experiments of BF-1 sample under UV light irradiation ($\lambda \leq 420$ nm). After 5 cycles, the BiF₃/BiOCl heterojunction (BF-1) nearly maintains the degradation activity of MO (Fig. 8a). After 5 cycles, the XRD patterns and SEM image of BF-1 have not changed (Fig. 8(b and c)), confirming a good stability of BiF₃/BiOCl heterojunction.

3.3.3. Photosensitization

In addition, in order to avoiding dye photosensitization, we have also test the photodegradation activity of 2-nitrophenol by the samples. Fig. 9(a,b) shows the degradation curves and reaction kinetic curves of 2-nitrophenol under UV light irradiation ($\lambda \leq 420$ nm). After being irradiated for 60 min, nearly 97% of 2-nitrophenol can be degraded by both BF-1 and BF-2 sample; in contrast, only 38%, 51% and 28% of 2-nitrophenol can be degraded by BF-0 (BiOCl), BF-3 and BF-4 (BiF₃) samples, respectively. Moreover, the degradation rates of BiF₃/BiOCl (BF-1 and BF-2) sample are 5.3 and 5.8 times higher than that of phase-pure BiOCl (BF-0) and BiF₃ (BF-4), respectively. It is obvious that BF-1 and BF-2 have higher photocatalytic activities, compared with pure BiOCl and BiF₃. The enhanced photocatalytic activity may be attributed to the formation of BiF₃/BiOCl heterojunction, which benefits the separation and transfer of charges.

3.4. A plausible photocatalytic mechanism of BiF₃/BiOCl heterojunctions

From the results above, the generation and separation efficiency of photogenerated charges plays a key role in the photocatalytic activity. Herein, we hold that BiF₃/BiOCl heterojunction has significantly improved the charge separation and transfer efficiency, because their energy bands are well matched: the CBs of BiOCl and

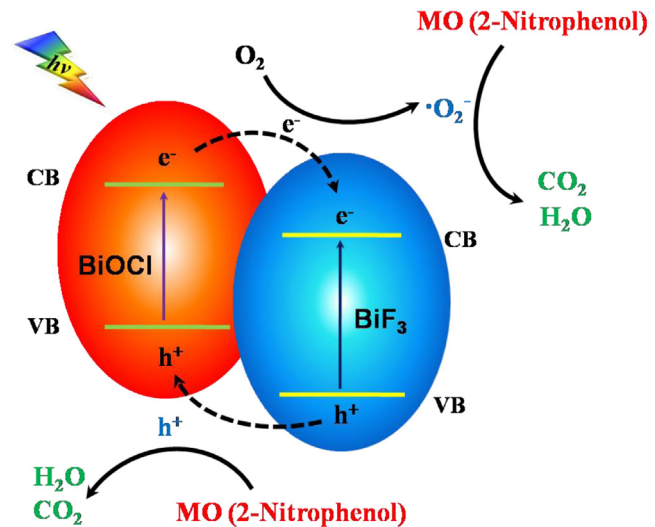


Fig. 10. Schematic diagram of photogenerated charges transfer and photocatalytic mechanism over the BiF₃/BiOCl heterojunctions.

BiF₃ are 0.4 and 2.02 eV, respectively; while their VBs are 3.91 and 6.04 eV, respectively. As illustrated in Fig. 10, a stable BiF₃/BiOCl heterojunction is easy to form [45,60]. It is well known that BiOCl has a unique layered structure, which is composed of $[\text{Bi}_2\text{O}_2]^{2+}$ layers interleaved with Cl layers. Thus a strong bulk internal electric field can form between anion layers and cation layers, which favors for the charge separation. Besides, an interfacial electric field is easy to form between BiF₃ and BiOCl due to their well matched energy bands. Therefore, under UV light irradiation, the photogenerated electrons at the CB of BiOCl would transfer to the CB of BiF₃; meanwhile the generated holes at the VB of BiF₃ would migrate to the VB of BiOCl driven by both bulk internal electric field and interfacial electric field. Herein, the recombination of electrons and holes would be obviously inhibited, and the separation efficiency would be improved.

The electrons at the surface of the BiF₃/BiOCl heterojunction will react with O_2 (dissolved oxygen) to form superoxide radical ($\cdot\text{O}_2^-$). The trapping experiment for hydroxyl radical ($\cdot\text{OH}$) indicates that $\cdot\text{OH}$ has nearly no influence on the photocatalytic activity. Hence, we could speculate that the generated superoxide radicals and holes may not further react with H_2O to form hydroxyl radicals ($\cdot\text{OH}$) as the reactive species. Herein, we could believe that the holes and superoxide radicals will directly oxidize the MO and 2-nitrophenol (as demonstrated by the trapping experiment, Fig. 7c and Fig. S7), and the organic molecules are mineralized from small

molecules like CO_2 and H_2O , etc. (as demonstrated by the TOC results, Fig. 6c). But, the real photocatalytic process on $\text{BiF}_3/\text{BiOCl}$ heterojunction still needs further study.

4. Conclusions

In conclusion, $\text{BiF}_3/\text{BiOCl}$ heterojunction can be prepared by a simple post-synthesis method, whose optimal molar ratio of BiF_3 to BiOCl is 38%. For BiOCl , the photogenerated electrons mainly move to the surface and accumulate on the surface; for $\text{BiF}_3/\text{BiOCl}$ heterojunction, the electrons and holes can both move to the surface and accumulate on the surface. However, nearly no electrons or holes can accumulate on the surface of BiF_3 . This could help us to intensively understand the charge transfer behavior from bulk to surface of semiconductor. Additionally, the trapping experiments confirm that the holes are the major oxidative species for BiOCl whereas both hydroxyl radicals and holes are the major active oxidative species for BiF_3 sample. However, the MO degradation over $\text{BiF}_3/\text{BiOCl}$ heterojunction is driven mainly by the superoxide radicals and holes. The greatly improved degradation activity of $\text{BiF}_3/\text{BiOCl}$ heterojunction is mainly attributed to the improved charges separation and transfer efficiency, which has been ascribed to the synergetic effect of surface electric field, bulk internal electric field and interfaces electric field.

Acknowledgements

This work is financially supported by National Science Foundation of China (21377060), Scientific Research Foundation for the Returned Overseas Chinese Scholars of State Education Ministry (20121707), Six Talent Climax Foundation of Jiangsu (20100292), Natural Science Foundation of Jiangsu province (BK2012464), the Key Project of Environmental Protection Program of Jiangsu (2013005), the Project Funded by the Science and Technology Infrastructure Program of Jiangsu (BM201380277), and A Project Funded by the Priority Academic Program Development of Jiangsu Higher Education Institutions (PAPD) sponsored by SRF for ROCS, SEM (2013S002).

Appendix A. Supplementary data

Supplementary data associated with this article can be found, in the online version, at <http://dx.doi.org/10.1016/j.apcatb.2016.12.062>.

References

- [1] A. Fujishima, Nature 238 (1972) 37–38.
- [2] A. Kudo, Int. J. Hydrogen Energy 31 (2006) 197–202.
- [3] H.F. Cheng, B.B. Huang, Y. Dai, Nanoscale 6 (2014) 2009–2026.
- [4] P. Cui, J. Wang, Z. Wang, J. Chen, X. Xing, L. Wang, R. Yu, Nano Res. 9 (2016) 593–601.
- [5] Q. Xu, W. Lei, X. Li, X. Qi, J. Yu, G. Liu, P. Zhang, Environ. Sci. Technol. 48 (2014) 9702–9708.
- [6] J.J. Branch, B.M. Bartlett, Chem. Mater. 27 (2015) 7207–7217.
- [7] Y. Li, W. Xie, X. Hu, G. Shen, X. Zhou, Y. Xiang, X. Zhao, P. Fang, Langmuir 26 (2009) 591–597.
- [8] Y.P. Bi, S.X. Ouyang, N. Umezawa, J.Y. Cao, J.H. Ye, J. Am. Chem. Soc. 133 (2011) 6490–6492.
- [9] J. Wang, F. Teng, M. Chen, J.J. Xu, Y.Q. Song, X.L. Zhou, CrystEngComm 15 (2013) 39–42.
- [10] F. Teng, Z.L. Liu, A. Zhang, M. Li, Environ. Sci. Technol. 49 (2015) 9489–9494.
- [11] Y. Shi, H. Li, L. Wang, W. Shen, H. Chen, ACS Appl. Mater. Inter. 4 (2012) 4800–4806.
- [12] D. Wang, R. Li, J. Zhu, J. Shi, J. Han, X. Zong, C. Li, J. Phys. Chem. C 116 (2012) 5082–5089.
- [13] Z.F. Huang, L. Pan, J.J. Zou, X. Zhang, L. Wang, Nanoscale 6 (2014) 14044–14063.
- [14] J. Tian, Y. Sang, G. Yu, H. Jiang, X. Mu, H. Liu, Adv. Mater. 25 (2013) 5075–5080.
- [15] Y. Liu, W. Yao, D. Liu, R. Zong, M. Zhang, X. Ma, Y. Zhu, Appl. Catal. B: Environ. 163 (2015) 547–553.
- [16] H. Huang, X. Li, J. Wang, F. Dong, P.K. Chu, T. Zhang, Y. Zhang, ACS Catal. 5 (2015) 4094–4103.
- [17] H. Huang, J. Wang, F. Dong, Y. Guo, N. Tian, Y. Zhang, T. Zhang, Cryst. Growth Des. 15 (2015) 534–537.
- [18] X. Zhang, Z.H. Ai, F.L. Jia, L.Z. Zhang, J. Phys. Chem. C 112 (2008) 747–753.
- [19] J. Li, L. Cai, J. Shang, Y. Yu, L. Zhang, Adv. Mater. 28 (2016) 4059–4064.
- [20] H. Li, J. Shang, Z. Ai, L. Zhang, J. Am. Chem. Soc. 137 (2015) 6393–6399.
- [21] R. Qiao, M. Mao, E. Hu, Y. Zhong, J. Ning, Y. Hu, Inorg. Chem. 54 (2015) 9033–9039.
- [22] C.Y. Wang, X. Zhang, X.N. Song, W.K. Wang, H.Q. Yu, ACS Appl. Mater. Interfaces 8 (2016) 5320–5326.
- [23] M. Gao, D. Zhang, X. Pu, H. Li, W. Li, X. Shao, J. Dou, Sep. Purif. Technol. 162 (2016) 114–119.
- [24] J. Li, Y. Yu, L.Z. Zhang, Nanoscale 6 (2014) 8473–8488.
- [25] S. Yin, J. Di, M. Li, Y. Sun, J. Xia, H. Xu, H. Li, J. Mater. Sci. 51 (2016) 4769–4777.
- [26] W.T. Li, W.Z. Huang, H. Zhou, H.Y. Yin, Y.F. Zheng, X.C. Song, J. Alloys Compd. 638 (2015) 148–154.
- [27] J. Di, J. Xia, S. Yin, H. Xu, L. Xu, Y. Xu, M. He, H. Li, RSC Adv. 4 (2014) 14281–14290.
- [28] X. Zhang, L. Zhao, C. Fan, Z. Liang, P. Han, Physica B 407 (2012) 4416–4424.
- [29] S. Zhang, D. Wang, L. Song, Mater. Chem. Phys. 173 (2016) 298–308.
- [30] J. Di, J. Xia, M. Ji, B. Wang, S. Yin, Y. Huang, H. Li, Appl. Catal. B: Environ. 188 (2016) 376–387.
- [31] H. Li, L. Zhang, Nanoscale 6 (2014) 7805–7810.
- [32] S. Bai, X. Li, Q. Kong, R. Long, C. Wang, J. Jiang, Y. Xiong, Adv. Mater. 27 (2015) 3444–3452.
- [33] X. Yan, X. Zhu, R. Li, W. Chen, J. Hazard. Mater. 303 (2016) 1–9.
- [34] X. Chang, S. Wang, Q. Qi, M.A. Gondal, S.G. Rashid, S. Gao, P. Wang, Dalton Trans. 44 (2015) 15888–15896.
- [35] S. Weng, B. Chen, L. Xie, Z. Zheng, P. Liu, J. Mater. Chem. A. 1 (2013) 3068–3075.
- [36] T.B. Li, G. Chen, C. Zhou, Z.Y. Shen, R.C. Jin, J.X. Sun, Dalton Trans. 40 (2011) 6751–6758.
- [37] H.F. Cheng, B.B. Huang, X.Y. Qin, X.Y. Zhang, Y. Dai, Chem. Commun. 48 (2012) 97–99.
- [38] L.Q. Ye, J.Y. Liu, C.Q. Gong, L.H. Tian, T.Y. Peng, L. Zan, ACS Catal. 2 (2012) 1677–1683.
- [39] B.C. Cao, P. Dong, S. Cao, Y.H. Wang, J. Am. Ceram. Soc. 96 (2013) 544–548.
- [40] W. Shan, Y. Hu, Z. Bai, M. Zheng, C. Wei, Appl. Catal. B: Environ. 188 (2016) 1–12.
- [41] L. Yu, X. Zhang, G. Li, Y. Cao, S. Yu, D. Li, Appl. Catal. B: Environ. 187 (2016) 301–309.
- [42] R. Fu, X. Zeng, L. Ma, S. Gao, Q. Wang, Z. Wang, J. Lu, J. Power Sources 312 (2016) 12–22.
- [43] S. Ning, L. Ding, Z. Lin, Q. Lin, H. Zhang, H. Lin, X. Wang, Appl. Catal. B: Environ. 185 (2016) 203–212.
- [44] C. Feng, F. Teng, Z. Liu, C. Chang, Y. Zhao, S. Wang, Y. Zhu, J. Mol. Catal. A: Chem. 401 (2015) 35–40.
- [45] N. Li, X. Hua, K. Wang, Y. Jin, J. Xu, M. Chen, F. Teng, Dalton Trans. 43 (2014) 13742–13750.
- [46] P. Wang, T.F. Xie, H.Y. Li, L. Peng, Y. Zhang, T.S. Wu, D.J. Wang, Chem. Eur. J 15 (2009) 4366–4372.
- [47] H. Fan, T. Jiang, H. Li, D. Wang, L. Wang, J. Zhai, T. Xie, J. Phys. Chem. C 116 (2012) 2425–2430.
- [48] Z. Zhang, W. Wang, L. Wang, S. Sun, ACS Appl. Mater. Interfaces 4 (2012) 593–597.
- [49] J. Xu, F. Teng, C. Xu, Y. Yang, L. Yang, Y. Kan, J. Phys. Chem. C 119 (2015) 13011–13020.
- [50] X. Zheng, D. Li, X. Li, J. Chen, C. Cao, J. Fang, J. Wang, Y. He, Y. Zheng, Appl. Catal. B: Environ. 168 (2015) 408–415.
- [51] Y. Ohko, K. Hashimoto, A. Fujishima, J. Phys. Chem. A 101 (1997) 8057–8062.
- [52] M. Long, W. Cai, J. Cai, B. Zhou, X. Chai, Y. Wu, J. Phys. Chem. B 110 (2006) 20211–20216.
- [53] Y.Y. Zhu, Q. Ling, Y.F. Liu, H. Wang, Y.F. Zhu, Phys. Chem. Chem. Phys. 17 (2015) 933–940.
- [54] Y.D. Hou, A.B. Laursen, J.S. Zhang, G.G. Zhang, Y.S. Zhu, X.C. Wang, S. Dahi, I. Chorkendorff, Angew. Chem. Int. Ed. 52 (2013) 621–3625.
- [55] H. Kim, P. Borse, W. Choi, J. Lee, Angew. Chem. Int. Ed. 44 (2005) 4585–4589.
- [56] N. Kavcar, Sol. Energy Mater. Sol. Cells 52 (1998) 183–195.
- [57] D.P. Norton, Y.W. Heo, M.P. Iville, K. Ip, S.J. Pearson, M.F. Chisholm, T. Steiner, Mater. Today 7 (2004) 34–40.
- [58] J. Seo, P. Roushan, H. Beidenkopf, Y.S. Hor, R.J. Cava, A.T. Yazdani, Nature 466 (2010) 343–346.
- [59] L. Ye, K. Deng, F. Xu, L. Tian, T. Peng, L. Zan, Phys. Chem. Chem. Phys. 14 (2012) 82–85.
- [60] Y.H. Hong, H.Y. Guai, S. Liu, R.Y. Jiang, Ceram. Int. 40 (2014) 9095–9100.